

RESEARCH LETTER

10.1002/2013GL058955

Key Points:

- Climate response depends strongly on spatial pattern of ocean heat uptake
- Different radiative feedbacks govern transient and equilibrium CO₂ warming
- Results are robust across an ensemble of aquaplanet climate models

Supporting Information:

- Readme
- Figure S1
- Figure S2

Correspondence to:

B. Rose,
brose@albany.edu

Citation:

Rose, B. E. J., K. C. Armour, D. S. Battisti, N. Feldl, and D. D. B. Koll (2014), The dependence of transient climate sensitivity and radiative feedbacks on the spatial pattern of ocean heat uptake, *Geophys. Res. Lett.*, *41*, 1071–1078, doi:10.1002/2013GL058955.

Received 4 DEC 2013

Accepted 13 JAN 2014

Accepted article online 24 JAN 2014

Published online 15 FEB 2014

The dependence of transient climate sensitivity and radiative feedbacks on the spatial pattern of ocean heat uptake

Brian E. J. Rose¹, Kyle C. Armour², David S. Battisti³, Nicole Feldl⁴, and Daniel D. B. Koll⁵

¹Department of Atmospheric and Environmental Sciences, University at Albany, State University of New York, Albany, New York, USA, ²Department of Earth, Atmospheric and Planetary Sciences, MIT, Cambridge, Massachusetts, USA, ³Department of Atmospheric Sciences, University of Washington, Seattle, Washington, USA, ⁴Division of Geological and Planetary Sciences, Caltech, Pasadena, California, USA, ⁵Department of the Geophysical Sciences, University of Chicago, Chicago, Illinois, USA

Abstract The effect of ocean heat uptake (OHU) on transient global warming is studied in a multimodel framework. Simple heat sinks are prescribed in shallow aquaplanet ocean mixed layers underlying atmospheric general circulation models independently and combined with CO₂ forcing. Sinks are localized to either tropical or high latitudes, representing distinct modes of OHU found in coupled simulations. Tropical OHU produces modest cooling at all latitudes, offsetting only a fraction of CO₂ warming. High-latitude OHU produces three times more global mean cooling in a strongly polar-amplified pattern. Global sensitivities in each scenario are set primarily by large differences in local shortwave cloud feedbacks, robust across models. Differences in atmospheric energy transport set the pattern of temperature change. Results imply that global and regional warming rates depend sensitively on regional ocean processes setting the OHU pattern, and that equilibrium climate sensitivity cannot be reliably estimated from transient observations.

1. Introduction

Ocean heat uptake (OHU) has long been recognized as critical in setting the pace of climate change [Hansen *et al.*, 1985; Raper *et al.*, 2002]. The deep oceans are warmed through a variety of vertical heat transport processes [Gregory, 2000] that delay warming at the surface. Ocean temperature trends over recent decades indicate 0.5–1 W m⁻² global mean OHU [Hansen *et al.*, 2005; Lyman *et al.*, 2010; Balmaseda *et al.*, 2013]. The Earth is in radiative disequilibrium—and cooler than it would otherwise be—due to OHU offsetting a substantial portion of the roughly 2 W m⁻² present radiative forcing [IPCC, 2013]. Such is the traditional view of the role of OHU in setting transient climate sensitivity.

However, observations [Yu and Weller, 2007] and coupled general circulation model (GCM) simulations [Winton *et al.*, 2010; Bitz *et al.*, 2012] suggest that the geographic pattern of OHU is far from uniform or steady (see supporting information). A key question, then, is whether the global mean surface warming is sensitive to the pattern of OHU. Winton *et al.* [2010] introduce an “efficacy” parameter in the global mean energy budget to account for the intermodel spread in sensitivity of global surface temperature to OHU relative to radiative forcing and find the largest efficacy when OHU occurs preferentially at high latitudes [see also Bitz *et al.*, 2012]. Armour *et al.* [2013] offer an explanation in terms of the spatial pattern of atmospheric radiative feedback (the local linearized relationship between top-of-atmosphere (TOA) radiative response and surface warming). To the extent that suppression of surface warming by OHU is primarily local, we expect OHU to affect global mean temperature most strongly when colocated with regions of net positive (destabilizing) local feedback, typically also found at high latitudes [Armour *et al.*, 2013]. However, it is not clear that the far-field temperature effects of OHU should be negligible, nor that local radiative feedbacks should remain constant in time as assumed by Armour *et al.* [2013]. An evolving OHU pattern may influence atmospheric structure sufficiently to modify local feedbacks.

Here we study the direct connection between the spatial pattern of OHU, radiative feedback, and temperature response. We analyze a series of idealized mixed layer aquaplanet model simulations, wherein we prescribe OHU through a “q flux” that removes heat from the ocean mixed layer with a particular geographic pattern, mimicking the deep ocean’s role in the coupled climate system. We take advantage of the separation of atmospheric and oceanic timescales by studying the climatic significance of the spatial pattern of

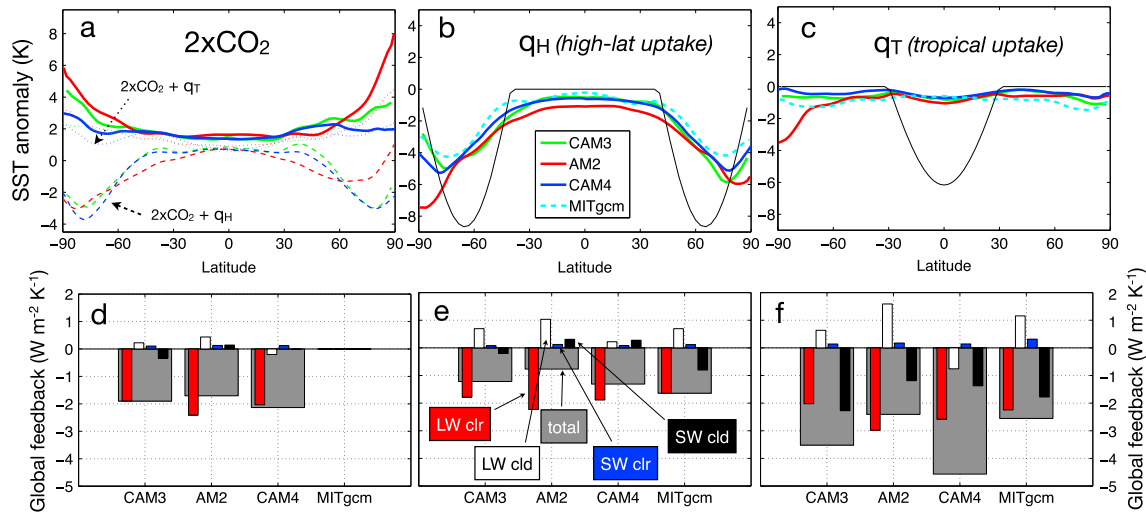


Figure 1. Multimodel study of climate sensitivity to prescribed ocean heat sinks compared to greenhouse gas forcing. (a–c) Equilibrium SST anomalies relative to control simulations for each model. Figure 1a shows the response to $2 \times \text{CO}_2$ alone (solid) and the responses to combined $2 \times \text{CO}_2$ plus prescribed OHU in the high latitudes (q_H , equation (1), dashed) and tropics (q_T , equation (2), dotted). Figures 1b and 1c show the responses to OHU alone, with the prescribed heat sinks also plotted in W m^{-2} (thin grey). (d–f) Estimates of global mean feedback λ_G under the three single-forcing scenarios. For each model and each forcing, the total feedback is shown in thick grey bars, along with its decomposition into LW and SW clear and cloudy sky components.

OHU in a quasi-equilibrium framework. We compare two distinct OHU patterns, one centered at subpolar high latitudes ($\equiv q_H$) and the other localized within the tropics ($\equiv q_T$), that each produce the same area-weighted global mean OHU ($\equiv A_{up}$, which we set to 2 W m^{-2} , roughly half the radiative forcing from a doubling of CO_2). The patterns are steady in time, symmetric about the equator and zonally, and varying in latitude ϕ by

$$q_H = \min \left(0, -\frac{299A_{up}}{90 \cos(\frac{2\pi}{9})} \sin \left(\frac{18}{5} \left(|\phi| - \frac{2\pi}{9} \right) \right) \right) \quad (1)$$

$$q_T = \min \left(0, -\frac{16A_{up}}{3\sqrt{3}} \cos(3\phi) \right) \quad (2)$$

q_H peaks around 9 W m^{-2} at 65° latitude and is zero at the poles and equatorward of 40° , while q_T peaks around 6 W m^{-2} at the equator and is zero poleward of 30° (Figures 1b and 1c). These OHU patterns broadly capture those found within coupled GCMs under transient warming (see supporting information).

We address two sets of questions. First, how does the spatial pattern of OHU affect the surface temperature response (both global mean and spatial pattern)? And second, can these differences be understood in terms of fixed underlying local radiative feedbacks, or are the feedbacks themselves sensitive to the OHU pattern? We prescribe q_T and q_H independently and in conjunction with a doubling of CO_2 . These simulations are thus a direct test of the degree to which OHU can compensate for an imposed radiative forcing, depending on its geographic structure. We propose that they serve as a challenge to the traditional, global mean view of OHU and as a guide to understanding the complex role of oceans in regional and global climate change.

2. Model Intercomparison

In order to assess the robustness of our results, we use four different GCMs (Table 1), all configured as idealized slab ocean aquaplanets. CAM3 [Collins *et al.*, 2004] is the atmospheric component of National Center for Atmospheric Research’s Community Climate System Model 3 (CCSM3); Community Atmosphere Model 4 (CAM4) uses a newer dynamical core and updated deep convection and cloud fraction schemes [Neale *et al.*, 2013]; AM2.1 is the atmospheric component of GFDL’s CM2.1 model [Delworth *et al.*, 2006]. MITgcm is a five-level model with simplified moist physical parameterizations [Molteni, 2003; Rose and Ferreira, 2013]. This model’s crude four-band radiative scheme precludes carrying out a $2 \times \text{CO}_2$ experiment.

Our aquaplanet setup follows Lee *et al.* [2008] and is similar to the “aqua-planet experiment” of Neale and Hoskins [2000], except that we use energetically consistent mixed layer ocean models with prognostic sea

Table 1. Summary of Models Used and Their Global-Mean SST Anomalies in Each Experiment^a

Model	Horizontal Grid	Levels	$2 \times \text{CO}_2$	q_H	q_T	$2 \times \text{CO}_2 + q_H$	$2 \times \text{CO}_2 + q_T$	Standard
CAM3	spectral T42	26	1.8	-1.6	-0.6	0.2	1.2	2.7
AM2.1	finite volume $2.0^\circ \times 2.5^\circ$	24	1.9	-2.1	-0.8	-0.2	1.3	3.4
CAM4	finite volume $1.9^\circ \times 2.5^\circ$	26	1.7	-1.5	-0.4	0.0	1.2	3.1
MITgcm	cubed-sphere C32	5	-	-1.2	-0.8	-	-	-
Mean			1.8	-1.7	-0.6	0.0	1.2	3.1

^aGlobal mean SST anomalies are expressed relative to control runs for each model, in K. Multimodel mean values are taken over the three full physics models (CAM3, AM2.1, CAM4). All simulations use model default parameters except as noted in the text. The final column lists the published equilibrium climate sensitivities for the standard configurations of these models [Randall et al., 2007; Bitz et al., 2012].

surface temperature (SST). Perpetual equinox insolation is prescribed with solar constant 1365 W m^{-2} . Mixed layer depth is 10 m. Sea surface albedo is fixed at 0.1. Control simulations are performed with 348 ppmv CO_2 , 1650 ppbv CH_4 , and 306 ppbv N_2O (all other greenhouse gases set to zero). Ozone has a prescribed steady symmetric distribution [Blackburn and Hoskins, 2013]. Sea ice is omitted but SST below freezing is permitted (no surface albedo feedback). Each simulation (control and forced) is integrated to equilibrium, at least 10 years.

The climatic impacts of CO_2 and OHU are shown in Figures 1a–1c as time- and zonal mean SST anomalies relative to each model's control simulation. The control climates differ between models but feature warm equatorial SSTs around 30°C and cold polar SSTs near -40°C . The large equator-to-pole SST gradient is a consequence of equinoctial insolation. The slight interhemispheric asymmetries in Figure 1 are all due to internal model variability.

Figure 1a shows warming from $2 \times \text{CO}_2$ (equilibrium climate sensitivity) as well as the combined effects of $2 \times \text{CO}_2$ and OHU (analogous to transient climate sensitivity). CO_2 alone (solid lines) produces warming everywhere, with some spread in the amount of polar amplification. Global mean $2 \times \text{CO}_2$ warming is about 1.8 K in our aquaplanets—weaker and with less intermodel spread than the standard configurations of these models (Table 1), suggesting that we are undersampling the uncertainty in climate feedback. The deliberate elimination of surface ice and snow from our simulations likely contributes to this.

Figure 1a also shows that OHU mitigates the CO_2 warming, as expected. However, this effect is very sensitive to the location of OHU. For high-latitude OHU (q_H), only 2 W m^{-2} of global OHU is necessary to fully cancel 4 W m^{-2} of greenhouse gas warming (Table 1, dashed curves in Figure 1a). The same OHU limited to the tropics (q_T , dotted curves) mitigates global warming by only a third (about 0.6°C , Table 1). The cooling due to OHU alone (Figures 1b and 1c) is similarly dependent on the spatial pattern of the uptake. In the global mean, we find three times more cooling from q_H as from q_T (Table 1). The spatial pattern of the cooling is very different: roughly globally uniform for q_T (Figure 1c) and highly amplified at high latitudes for q_H (Figure 1b). All these results are remarkably robust across models.

Another remarkable result is the linearity of the model responses: SST anomalies from combined CO_2 and OHU forcing are closely approximated by the sum of the responses to individual forcings, both globally and locally (see Table 1, and the supporting information). We take the linearity as justification for studying the responses to CO_2 and OHU in isolation. While our primary interest is in the combined effects of CO_2 and OHU (our analog of transient climate sensitivity), the rest of this paper will simply compare the warming pattern from $2 \times \text{CO}_2$ to the cooling patterns due to q_H and q_T .

3. Radiative Feedback Analysis

Our analysis is framed around a time mean and zonal mean TOA energy budget for perturbations to the control climate:

$$H(\phi) = \lambda(\phi)T(\phi) + R(\phi) - \nabla \cdot \mathbf{F}(\phi) \quad (3)$$

where H is the prescribed deep ocean heat sink ($H > 0$), \mathbf{F} is the anomalous northward atmospheric energy transport, and $\lambda(\phi)T(\phi) + R(\phi)$ is the net anomalous downwelling radiation linearized about the local SST anomaly. Thus, $R(\phi)$ is the radiative forcing ($R > 0$ for $2 \times \text{CO}_2$), while $\lambda(\phi)$ is the local climate feedback ($\lambda < 0$

for stabilizing feedback), which we decompose into additive longwave (LW) and shortwave (SW) contributions from clear and cloudy sky. We also define the usual global climate feedback as $\lambda_G = (\overline{H} - \overline{R})/\overline{T}$, with the overbars denoting an area-weighted global mean. Global and local feedbacks are thus related by [e.g., Armour *et al.*, 2013]

$$\lambda_G = \overline{\lambda(\phi)T^*(\phi)}, \quad T^*(\phi) \equiv \frac{T(\phi)}{\overline{T}} \quad (4)$$

In our OHU-only simulations, $R = 0$, $H(\phi)$ is prescribed, and $\lambda(\phi)$ can be estimated directly from anomalous SST and TOA radiative fluxes at equilibrium. A different method must be used for $2 \times \text{CO}_2$, as the TOA radiative fluxes include contributions from both feedback and forcing. We estimate $\lambda(\phi)$ and $R(\phi)$ for each model as the slope and intercept (respectively) of the local regression between TOA radiation and SST anomalies at each latitude under *transient* warming [Crook *et al.*, 2011; Gregory *et al.*, 2004]. To generate sufficient data for this analysis, we set the mixed layer depth to 200 m, initialize each model with its control SST, and integrate for 40 years following abrupt CO_2 doubling. λ_G is then calculated from equation (4) using the equilibrium SST anomalies.

3.1. Global Mean Feedback

Multimodel estimates of λ_G are shown in Figures 1d–1f (thick grey bars) for the three single-forcing scenarios ($2 \times \text{CO}_2$, q_H , q_T). λ_G is very sensitive to the type of forcing. There is intermodel spread in the feedback estimate for each scenario, but the gross differences in overall feedback between the different forcing scenarios is robust. All models in our ensemble show that λ_G is 3 to 4 times more negative under q_T than q_H , consistent with the stronger global SST response to high-latitude OHU (Figures 1b and 1c). λ_G under $2 \times \text{CO}_2$ is intermediate between these two extremes. These results are consistent with Colman and McAvaney [1997], who found less negative global feedback with more strongly polar-amplified warming in specified SST experiments.

The decomposition in Figures 1d–1f (thin colored bars) shows that the robustly less negative λ_G under q_H relative to $2 \times \text{CO}_2$ is largely due to cloud effects, with contributions from both LW (white bars) and SW (black bars). The strongly negative λ_G under q_T is largely due to SW cloud effects, which are substantially more negative in every model in this scenario, while there is greater intermodel spread in the LW cloud response. In all models the clear sky LW component (red bars) is more negative under q_T and less negative under q_H relative to $2 \times \text{CO}_2$.

Figure 1 establishes that the intermodel spread in λ_G and $T^*(\phi)$ for each forcing is substantially smaller than the model mean differences between these forcing scenarios. We therefore suppose that model-independent insight into the reasons for the different sensitivities can be derived from a detailed analysis of a single model. In the following we examine the spatial structure of the response in CAM4, which features the most up-to-date physical parameterizations in our model ensemble. Key results and conclusions are qualitatively reproduced in the other models.

3.2. Local Energy Budget and Feedback in CAM4

We wish to understand whether the differences in λ_G in response to different forcings can be explained in the context of fixed $\lambda(\phi)$ and different temperature patterns $T^*(\phi)$ [Armour *et al.*, 2013], or whether $\lambda(\phi)$ itself changes substantially under different forcings. We now analyze the TOA energy budget (equation (3)) for CAM4 under the three single-forcing scenarios in Figures 2a–2c. For the OHU-only experiments, net radiation and heat transport divergence balance the imposed heat sink at each latitude. For $2 \times \text{CO}_2$, heat transport divergence balances net radiation (forcing plus feedback) everywhere.

From Figure 2b, q_H is largely balanced by local radiation, dominated by the clear sky LW component; high-latitude cloud changes have nearly compensating LW and SW effects. Heat transport is secondary in this case. Heat transport and local radiation are roughly equally important in balancing the forcing under q_T . Tropical OHU efficiently cools remote latitudes while high-latitude OHU does not. This is consistent with the strongly polar-amplified cooling under q_H versus the globally uniform cooling under q_T .

Figures 2d–2f show the anomalous northward heat transport \mathbf{F} decomposed into components due to moisture (latent heat) and dry static energy. The weakness of $\nabla \cdot \mathbf{F}$ under q_H is associated with a near-cancellation of the dry and moist components of \mathbf{F} across the midlatitudes. Under q_T , there are large changes in the partition of \mathbf{F} across the tropics consistent with weakened poleward energy transport by the Hadley circulation, but \mathbf{F} is dominated by latent heat in the extratropics. Under $2 \times \text{CO}_2$ there are partially compensating

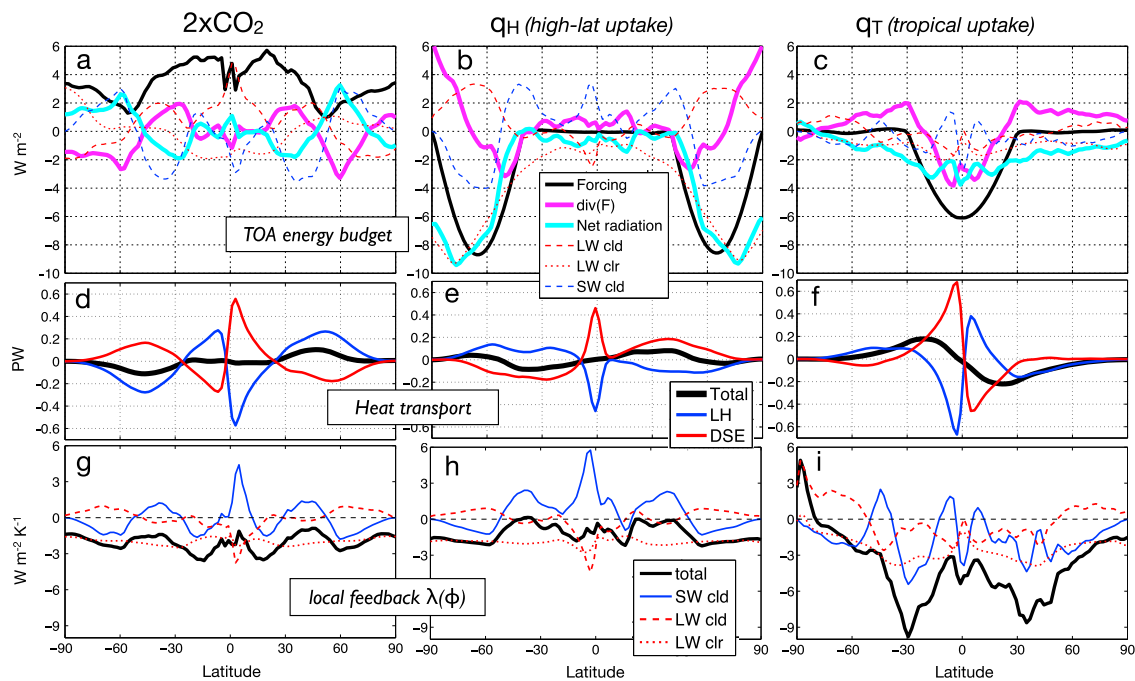


Figure 2. Spatial structure of the energy budget for CAM4 under the three forcing scenarios. (a–c) The forcing (black) plotted with anomalous heat transport divergence (magenta), net TOA radiation (cyan), and its breakdown into SW and LW components (the clear sky SW component is near zero and not shown). For $2 \times \text{CO}_2$ the forcing is estimated from the intercept of the regression line from the transient adjustment of the deep slab. (d–f) Anomalous northward energy flux, decomposed into latent heat and dry static energy components. (g–i) Local feedback $\lambda(\phi)$ for CAM4. In all cases the SW clear sky component is very small and not shown. Different methods are used to calculate $\lambda(\phi)$ for $2 \times \text{CO}_2$ and OHU-only simulations; see text for details.

changes in the dry and moist components but an overall increase in the poleward energy flux scaling with the moist component. This is consistent with the polar-amplified warming pattern [Alexeev et al., 2005].

Figures 2g–2i show estimates of the net local feedback $\lambda(\phi)$ in CAM4, along with its breakdown into LW and SW clear and (residual) cloud-sky components (the clear sky SW component is positive but less than $0.2 \text{ W m}^{-2} \text{ K}^{-1}$ everywhere, not plotted). The different forcings excite very different local feedbacks; $\lambda(\phi)$ under both heat uptake scenarios differ substantially from the $2 \times \text{CO}_2$ case (which we will denote $\lambda_{2x}(\phi)$). Under q_H the feedback is more positive (closer to zero) compared to $\lambda_{2x}(\phi)$ everywhere equatorward of 50° , with the difference due primarily to a more positive SW cloud feedback. Under q_T , the shape of each feedback component is profoundly different and the total $\lambda(\phi)$ is substantially more negative than $\lambda_{2x}(\phi)$ everywhere except near the poles. A more negative clear sky LW component contributes to this pattern, but the largest difference is again found in the SW cloud component, which is strongly negative across the subtropics and at the equator. Explanations for the very different sensitivities are thus to be found in the cloud regimes of the subtropics and within the Intertropical Convergence Zone (ITCZ). SW cloud feedback is negative at high latitudes in all cases, attributable to an increase in optical thickness of cold clouds with temperature [Zelinka and Hartmann, 2012].

To summarize, our different forcing scenarios excite different feedback patterns, dominated by SW cloud effects. A mechanistic understanding of the dependence of feedback on forcing will focus on interactions between large-scale dynamics and cloud cover and will be reported elsewhere.

3.3. Efficacy of Ocean Heat Uptake

Our results show that the global cooling effect of OHU depends sensitively on its geographic structure. Moreover, we have identified a remarkable linearity in the responses to OHU and CO_2 , such that their combined effect on global mean temperature is approximately additive: $\bar{T} = \bar{T}_{\text{ohu}} + \bar{T}_{2x}$, where $\bar{T}_{\text{ohu}} = \bar{H} / \lambda_{\text{Gohu}}$ and $\bar{T}_{2x} = -\bar{R}_{2x} / \lambda_{\text{G}2x}$ are the global temperature responses to OHU and $2 \times \text{CO}_2$, respectively. The global

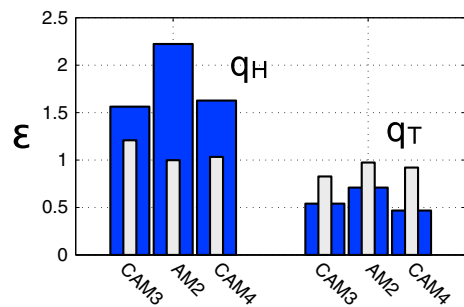


Figure 3. Efficacy of OHU relative to $2 \times \text{CO}_2$ in our two scenarios (larger ϵ indicates more global mean temperature change per W m^{-2} forcing). Blue bars show actual efficacy; white bars show the component due to differences in surface temperature patterns, neglecting the third term in equation (6). The difference between white and blue bars can be attributed to the differences in feedback $\lambda(\phi)$ in different scenarios.

mean energy budget for transient global warming can thus be written as

$$\epsilon \bar{H} = \lambda_{G2x} \bar{T} + \bar{R}_{2x}, \quad \epsilon \equiv \lambda_{G2x} / \lambda_{\text{Gohu}} \quad (5)$$

where ϵ represents relative influence of OHU on global temperature compared to CO_2 forcing—the “efficacy” of OHU as defined by *Winton et al.* [2010]. Efficacy is thus readily interpreted as the ratio of global radiative feedbacks operating under CO_2 and OHU. Through equation (4) we can further write

$$\epsilon^{-1} = 1 + \frac{\lambda_{2x}(\phi)}{\lambda_{G2x}} (T_{\text{ohu}}^*(\phi))' + \frac{(\lambda_{\text{ohu}}(\phi))'}{\lambda_{G2x}} T_{\text{ohu}}^*(\phi) \quad (6)$$

where primes refer to deviations of OHU-only feedback and temperature responses from their values under $2 \times \text{CO}_2$. Non-unit efficacy can thus result from different temperature patterns acting on fixed local feedbacks

$\lambda_{2x}(\phi)$ (the second term in equation (6), as discussed by *Armour et al.* [2013]) or by changes in the feedbacks themselves (third term in equation (6)).

ϵ is plotted in Figure 3 (blue bars); it is robustly greater than unity for q_H (1.6–2.2) and smaller than unity for q_T (0.5–0.6). The white bars show the component of efficacy due solely to changes in SST patterns (neglecting the third term in equation (6)). These are robustly close to unity in both scenarios. We conclude that changes in the local feedbacks primarily set the non-unit efficacy of the different OHU patterns.

While we emphasize the robust aspects of our results, we also find some intermodel spread. Figure 3 shows that ϵ for q_H differs between CAM3 and AM2 (1.56 versus 2.22). *Winton et al.* [2010] report consistent efficacy values for the corresponding coupled models CCSM3 and CM2.1 ($\epsilon = 1.65$ and 1.99 respectively) over periods of transient warming wherein OHU occurs preferentially in the sub-polar oceans.

3.4. Temperature Patterns in a Diffusive Model

Here we invoke a simple energy balance model (EBM) to further understand the spatial structure of SST anomalies under different forcings. Following *Hwang and Frierson* [2010] we assume that \mathbf{F} acts down the local gradient in near-surface moist static energy $m = c_p T + Lq$. We linearize for small perturbations as

$$\mathbf{F}(\phi) = -K \frac{d}{d\phi} (T(1 + f(\phi))), \quad f(\phi) \equiv \frac{Lr}{c_p} \frac{dq^*}{dT} \Big|_{T_{\text{ref}}(\phi)} \quad (7)$$

where q^* is the saturation specific humidity, r is the relative humidity, and $T_{\text{ref}}(\phi)$ is the zonal mean surface temperature from the control experiment. $f(\phi)$ depends only on the mean state (assuming no change in r) and decreases strongly with temperature; the CAM4 control simulation gives $f = 4$ at the equator and 0.03 at the poles. We set $K = 1.5 \times 10^6 \text{ W m}^{-1} \text{ K}^{-1}$ everywhere, consistent with *Hwang and Frierson* [2010].

Equations (7) and (3) define a boundary value problem ($\mathbf{F} = 0$ at the poles) for $T(\phi)$ given a forcing $R(\phi)$ and/or $H(\phi)$ and a feedback $\lambda(\phi)$. Figure 4 shows numerical solutions under our three single-forcing scenarios. We use the CAM4-derived $\lambda(\phi)$ for each scenario (Figures 2g–2i) and $R(\phi)$ for $2 \times \text{CO}_2$ as plotted in Figure 2a. We also plot solutions to the EBM using $\lambda = \lambda_{2x}(\phi)$ for the heat uptake cases (dashed curves).

While this model is very crude (reducing atmospheric dynamics to a 1-D linear diffusion operator), it captures the different spatial patterns of warming and cooling, regardless of whether we use an OHU-specific feedback pattern or simply $\lambda_{2x}(\phi)$. The nearly uniform cooling under q_T results from efficient export of the negative moist static energy anomaly out of the tropics due essentially to the strong background moisture gradient between low and high latitudes. The strongly polar-amplified cooling under q_H results from weak export of the negative moist static energy anomaly out of the high latitudes. We emphasize that no nonlinearity is necessary to capture this asymmetry [*Langen and Alexeev*, 2007].

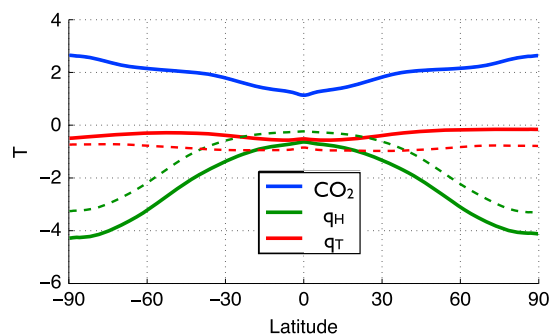


Figure 4. Zonal mean temperature anomalies from the diffusive EBM. Solid curves use CAM4-derived forcing and feedback diagnosed from each experiment (Figure 2). Dashed curves use $\lambda = \lambda_{2x}(\phi)$ for all cases.

4. Discussion and Conclusion

We summarize our results as follows: Tropical OHU produces a very modest cooling at all latitudes with weak efficacy relative to greenhouse gas forcing. High-latitude OHU produces three times more global cooling in a strongly polar-amplified pattern and features a large efficacy relative to greenhouse gas forcing. These results are robust across a small ensemble of GCMs (though all in consistent aquaplanet, perpetual equinox setups with no sea ice). We rationalize the very different spatial patterns of the responses in terms of the asymmetrical response of the atmospheric moisture transport to high- versus low-latitude energetic perturbations, consistent with previous studies [Alexeev et al., 2005; Hwang and Frierson, 2010].

Our results cannot be understood in terms of a fixed local feedback and differing spatial patterns of temperature change as was found in the CCSM4 model by Armour et al. [2013]. We find instead first-order changes in $\lambda(\phi)$ under different forcing scenarios. We have shown that cloud SW effects are a key contributor to changes in $\lambda(\phi)$. This is qualitatively consistent with Andrews et al. [2012] who find substantial SW cloud feedback changes in transient coupled GCM simulations.

A few caveats deserve mention here. We have excluded surface ice and snow from the models and thus eliminated a key positive feedback at high latitudes. We may therefore underestimate the (already very large) differences in responses to low- and high-latitude forcing. On the other hand, we may underestimate spatial variations in $\lambda(\phi)$ and the role of such variations in setting λ_G in the different scenarios. The perpetual equinox used in our calculations eliminates the seasonal cycle, pins the ITCZ permanently to the equator, and gives an overly strong equator-to-pole insolation gradient. It is not clear how all these inaccuracies (along with our idealized aquaplanet geometry) bias our results.

With these caveats in mind, we briefly address some implications of our results. Transient climate response is governed both by an evolving pattern of sea surface warming activating different local feedbacks and by changes in the local feedbacks themselves as the pattern of OHU slowly evolves. This casts doubt on the possibility of estimating the feedbacks governing transient climate change from equilibrium mixed layer models (as noted by Shell [2013]), and more importantly, of estimating equilibrium climate sensitivity from inherently transient climate observations. Regional ocean circulations (setting different patterns of OHU) may be an important source of intermodel spread in transient climate projections and of variability in the observed warming rate. For example, Kosaka and Xie [2013] attribute the recent hiatus in global warming to a La-Niña-like decadal depression of tropical Pacific SST (i.e., enhanced tropical OHU), which is found to exert a cooling of global extent, consistent with our q_T scenario. The large robust changes in SW cloud feedback under our different forcing scenarios illustrate an important role for the ocean in setting one of the main radiative control knobs on the global climate system. A follow-up study will seek a mechanistic explanation for this link.

References

Alexeev, V., P. Langen, and J. Bates (2005), Polar amplification of surface warming on an aquaplanet in “ghost forcing” experiments without sea ice feedbacks, *Clim. Dyn.*, *24*, 655–666.

Andrews, T., J. M. Gregory, M. J. Webb, and K. E. Taylor (2012), Forcing, feedbacks and climate sensitivity in CMIP5 coupled atmosphere-ocean climate models, *Geophys. Res. Lett.*, *39*, L09712, doi:10.1029/2012GL051607.

Armour, K. C., C. M. Bitz, and G. H. Roe (2013), Time-varying climate sensitivity from regional feedbacks, *J. Clim.*, *26*, 4518–4534.

Balmaseda, M. A., K. E. Trenberth, and E. Källén (2013), Distinctive climate signals in reanalysis of global ocean heat content, *Geophys. Res. Lett.*, *40*, 1754–1759, doi:10.1002/grl.50382.

Bitz, C., K. Shell, P. Gent, D. Bailey, G. Danabasoglu, K. Armour, M. Holland, and J. Kiehl (2012), Climate sensitivity of the Community Climate System Model, version 4, *J. Clim.*, *25*, 3053–3070.

Blackburn, M., and B. J. Hoskins (2013), Context and aims of the Aqua-Planet Experiment, *J. Meteor. Soc. Japan*, *91A*, 1–15, doi:10.2151/jmsj.2013-A01.

Acknowledgments

We thank C. Bitz, G. Roe, D. Hartmann, A. Pendergrass, D. Frierson, and A. Donohoe for discussions and two anonymous reviewers for helpful comments. D.S.B. and B.E.J.R. were partially supported by NSF Division of Earth Sciences Continental Dynamics Programs, awards 0908558 and 1210920. K.C.A. was supported by a James S. McDonnell Foundation Postdoctoral Fellowship. D.D.B.K. was supported by NSF DMS-0940261, which is part of the Mathematics and Climate Research Network.

The Editor thanks two anonymous reviewers for their assistance in evaluating this paper.

- Collins, W. D., et al. (2004), Description of the NCAR Community Atmosphere Model (CAM 3.0), *Tech. Rep. NCAR/TN-464+STR*, National Center for Atmospheric Research.
- Colman, R. A., and B. J. McAvaney (1997), A study of general circulation model climate feedbacks determined from perturbed sea surface temperature experiments, *J. Geophys. Res.*, *102*, 19,383–19,402.
- Crook, J. A., P. M. Forster, and N. Stuber (2011), Spatial patterns of modeled climate feedback and contributions to temperature response and polar amplification, *J. Clim.*, *24*, 3575–3592.
- Delworth, T. L., et al. (2006), GFDL's CM2 global coupled climate models. Part I: Formulation and simulation characteristics, *J. Clim.*, *19*, 643–674.
- Gregory, J. M. (2000), Vertical heat transports in the ocean and their effect on time-dependent climate change, *Clim. Dyn.*, *16*, 501–515.
- Gregory, J. M., W. J. Ingram, M. A. Palmer, G. S. Jones, P. A. Stott, R. B. Thorpe, J. A. Lowe, T. C. Johns, and K. D. Williams (2004), A new method for diagnosing radiative forcing and climate sensitivity, *Geophys. Res. Lett.*, *31*, L03205, doi:10.1029/2003GL018747.
- Hansen, J., G. Russell, A. Lacis, I. Fung, D. Rind, and P. Stone (1985), Climate response times: Dependence on climate sensitivity and ocean mixing, *Science*, *229*, 857–859, doi:10.1126/science.229.4716.857.
- Hansen, J., et al. (2005), Efficacy of climate forcings, *J. Geophys. Res.*, *110*, D18104, doi:10.1029/2005JD005776.
- Hwang, Y.-T., and D. M. W. Frierson (2010), Increasing atmospheric poleward energy transport with global warming, *Geophys. Res. Lett.*, *37*, L24807, doi:10.1029/2010GL045440.
- IPCC (2013), Summary for policymakers, in *Climate Change 2013: The Physical Science Basis. Contribution of Working Group I to the Fifth Assessment Report of the Intergovernmental Panel on Climate Change*, edited by T. Stocker et al., pp. 1–27, Cambridge Univ. Press, Cambridge, U. K.
- Kosaka, Y., and S.-P. Xie (2013), Recent global-warming hiatus tied to equatorial Pacific surface cooling, *Nature*, *501*, 403–407, doi:10.1038/nature12534.
- Langen, P. L., and V. A. Alexeev (2007), Polar amplification as a preferred response in an idealized aquaplanet GCM, *Clim. Dyn.*, *29*, 305–317.
- Lee, M.-I., M. J. Suarez, I.-S. Kang, I. M. Held, and D. Kim (2008), A moist benchmark calculation for atmospheric general circulation models, *J. Clim.*, *21*, 4934–4954.
- Lyman, J. M., S. A. Good, V. V. Gouretski, M. Ishii, G. C. Johnson, M. D. Palmer, D. M. Smith, and J. K. Willis (2010), Robust warming of the global upper ocean, *Nature*, *465*, 334–337, doi:10.1038/nature09043.
- Molteni, F. (2003), Atmospheric simulations using a GCM with simplified physical parameterizations. I: Model climatology and variability in multi-decadal experiments, *Clim. Dyn.*, *20*, 175–191.
- Neale, R. B., and B. J. Hoskins (2000), A standard test for AGCMs including their physical parametrizations: I: The proposal, *Atmos. Sci. Lett.*, *1*, 101–107, doi:10.1006/asle.2000.0022.
- Neale, R. B., J. Richter, S. Park, P. H. Lauritzen, S. J. Vavrus, P. J. Rasch, and M. Zhang (2013), The mean climate of the Community Atmosphere Model (CAM4) in forced SST and fully coupled experiments, *J. Clim.*, *26*, 5150–5168.
- Randall, D., et al. (2007), Climate models and their evaluation, in *Climate Change 2007: The Physical Science Basis. Contribution of Working Group I to the Fourth Assessment Report of the Intergovernmental Panel on Climate Change*, edited by S. Solomon et al., pp. 589–662, Cambridge Univ. Press, Cambridge, U. K.
- Raper, S. C. B., J. M. Gregory, and R. J. Stouffer (2002), The role of climate sensitivity and ocean heat uptake on AOGCM transient temperature response, *J. Clim.*, *15*, 124–130.
- Rose, B. E. J., and D. Ferreira (2013), Ocean heat transport and water vapor greenhouse in a warm equable climate: A new look at the low gradient paradox, *J. Clim.*, *26*, 2117–2136.
- Shell, K. M. (2013), Consistent differences in climate feedbacks between atmosphere-ocean GCMs and atmospheric GCMs with slab-ocean models, *J. Clim.*, *26*, 4264–4281.
- Winton, M., K. Takahashi, and I. M. Held (2010), Importance of ocean heat uptake efficacy to transient climate change, *J. Clim.*, *23*, 2333–2344.
- Yu, L., and R. A. Weller (2007), Objectively analyzed air-sea heat fluxes for the global ice-free oceans (1981–2005), *Bull. Amer. Meteor. Soc.*, *88*, 527–539.
- Zelinka, M. D., and D. L. Hartmann (2012), Climate feedbacks and their implications for poleward energy flux changes in a warming climate, *J. Clim.*, *25*, 608–624.